Mechanics of Materials 57 (2013) 15–29

Contents lists available at SciVerse ScienceDirect

Mechanics of Materials

journal homepage: www.elsevier.com/locate/mechmat

Fracture of a borosilicate glass under triaxial tension

V. Doquet *, N. Ben Ali, A. Constantinescu, X. Boutillon

Laboratoire de Mécanique des Solides, CNRS, Ecole Polytechnique Paristech, 91128 Palaiseau cedex, France

ARTICLE INFO

Article history:
Received 22 May 2012
Received in revised form 1 October 2012
Available online 1 November 2012

Keywords:
Brittle fracture
Thermal shock
Glass
Dynamic crack growth
Pores
Triaxial loading

ABSTRACT

The growth of 3D star-like cracks in a porous borosilicate glass was induced by "cold-to-hot" thermal shocks inducing triaxial tension in cylindrical specimens. As a consequence of the dynamic character of their propagation, the cracks had a "mirror-mist-hackle" aspect. Damage in unbroken specimens was characterized either by a modification of their vibration modes or by direct observations of sections. Pores were identified as the crack initiation sites. Thermo-mechanical simulations were done to analyze the stress field and its consequences, using either linear thermo-elasticity or an anisotropic continuum damage mechanics approach. Crack initiation was predicted at mid-height, at the center of the specimens, in accordance with the observations. The pore-induced stress concentration was shown to depend on the local stress triaxiality, as well as the stress intensity factor for an annular crack initiated from a pore. The capacity of the anisotropic continuum damage approach to predict qualitatively the influence of the shape of the specimen, as well as damage-induced modifications of vibration modes and the total fracture surface was demonstrated.

1. Introduction

Blocks of vitrified nuclear waste are prepared for deep underground storage by pouring a mixture of calcinated waste with molten sodium-borosilicate glass into steel canisters. During the cooling phase, temperature gradients (Barth et al., 2012) induce tri-axial tensile stresses and multiple cracking (Kamizono and Niwa, 1984; Faletti and Ethridge, 1988). When stored underground for thousands of years, the canisters might not remain water-tight, allowing leaching of the fractured glass by water. The risk of radionuclides release into the environment has thus to be assessed. The release rate would be directly proportional to the leachable surface, potentially increased by the presence of cracks. Therefore, the prediction of the increase in surface of a glass block associated with thermally-induced multiple cracking is a key environmental issue.

This study discusses crack initiation and growth in cylindrical specimens of an inactive but chemically representative glass during "cold-to-hot" thermal shocks. These shocks induce a triaxial tension representative of the loading conditions in the center of the glass blocks during cooling. The pertinence of "cold-to-hot" thermal shocks to investigate fracture in a cooling glass may at first seem questionable. But since the distribution of fracture strength of this glass was found to be independent of temperature in the range 20–500 °C (Dube et al., 2010) no history effect is suspected in terms of fracture. In other words, crack initiation is expected to be qualitatively similar under rising or decreasing temperature as long as the stress states in the initiation zone are similar. "Cold to hot" thermal shocks on laboratory specimens do not pretend to reproduce the complexity of potential crack paths in a solidifying glass block constrained by a steel canister but it allows an investigation of crack initiation under triaxial tension, while such a stress state is nearly impossible to achieve on a brittle material with conventional mechanical tests.

* Corresponding author. Tel.: +33 1 69 33 57 65; fax: +33 1 69 33 57 06.
E-mail address: doquet@lms.polytechnique.fr (V. Doquet).

0167-6636/$ - see front matter © 2012 Elsevier Ltd. All rights reserved.
http://dx.doi.org/10.1016/j.mechmat.2012.10.008

2. Experimental and numerical procedures

2.1. Experimental procedures

The material investigated is a non-translucent SON68 glass, containing mainly SiO_2 (45.5 weight%), B_2O_3 (14%), Na_2O (9,9%), other oxides, as well as Ruthenium and Palladium particles that emulate -from a chemical point of view-some heavy radionuclides. The glass is initially flawless, thanks to a slow cooling process. However, it contains some nearly spherical pores due to gas bubbles trapped in solidifying glass. Their diameter ranges from 100 to 800 μm. From the point of view of its defect content, defect size and distribution, this glass is not expected to be representative of the industrial material. The thermo-elastic properties of the glass were measured at different temperatures between 20 °C and 502 °C, the glass-transition temperature (Dube et al., 2010). Relaxation tests proved that below 350 °C, viscous effects are negligible during the short duration of the fracture tests reported below.

36 to 48.5 mm-high cylinders were cut from the 40 mm diameter glass rods supplied by the CEA (the French Agency for Atomic Energy). The specimens were equipped with three thermocouples glued in the center of each base and on the side surface, at mid-height with a ceramic paste for high-temperature bonding. The glass cylinders were cooled in a freezer during more than 12 h in order to have a homogeneous initial temperature and then, submitted to a "cold-to-hot" thermal shock, by quenching it into an oil bath pre-heated at a temperature ranging from 290 to 320 °C. During quenching, the axis of the specimens was kept vertical, so as to preserve the axial symmetry of the thermal and mechanical fields. The signals from the three thermocouples were recorded, to be used as boundary conditions in finite element simulations. Fig. 1 shows an example of recorded temperature evolutions.

Some specimens broke into several pieces (Fig. 2(a)) with a strong acoustic emission. In that case, the time elapsed since the specimen was plunged in oil was recorded and used to estimate the damage distribution at fracture from the model. For some specimens, the surface created by fracture was roughly evaluated by wrapping the pieces in an aluminum foil of known specific surface. Their surface was then obtained by weighting the foil and deducting the outer surface of the specimen. Clearly this provides a lower bound, since some pieces themselves contain small cracks that did not propagate all the way through (Fig. 2(b)). To refine this evaluation, the fragments containing arrested cracks were dipped in a white-colored solution (a colloidal silica suspension) during several hours to mark the boundary of thermal-shock induced cracks before breaking the pieces open and repeating the measurement on the colored areas.

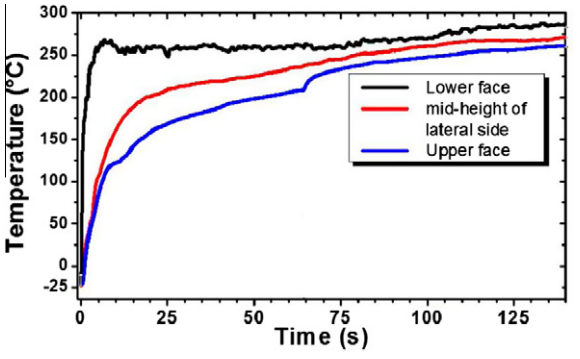

Fig. 1. Example of temperature evolutions recorded during a thermal shock.

Two series of vibration tests have been performed on the glass cylinders that did not break, before and after the thermal shock, in order to evaluate the thermal-shock-induced damage from the variation of the eigenfrequencies of internal solid waves. A reduction in the eigenfrequencies (Fig. 3(b)) reveals a loss of stiffness due to damage, which can be predicted using continuum damage mechanics (denoted below by CDM). The comparison of predicted and measured modifications in eigenfrequency is an efficient way to evaluate the pertinence of a CDM model, as already shown by Dube et al. (2010).

The cylinders were thus equipped with two piezo-electric sensors (Physical Acoustics Corporation), one (S9223 – sensitivity 1 V/μbar, frequency range: 30–1000 kHz) at the center of the bottom-face, the other (NANO30 – sensitivity 1 V/μbar, frequency range: 50–900 kHz) at mid-height. The cylinders were put on a soft foam pad (acting as a free boundary condition for the waves in the cylinder) and waves were impulsively excited by a Hsu-Nielsen source (brittle fracture of a 2H graphite lead, 0.5 mm in diameter, in a special fitting, according to ASTM976 standard) against the top-face. Response signals (Fig. 3(a)) were recorded during 8 ms by a numerical oscilloscope (Nicolet 490, 12-bit ADC) at a sampling frequency of 5 MHz (40,000 datapoints).

Longitudinal and transverse sections of unbroken specimens were also prepared for direct observations of damage with an optical digital microscope, also used for fractographic observations of broken specimens.

2.2. Numerical procedures

Axial symmetric finite element computations were performed to simulate quenching and evaluate the resulting damage considering a cylindrical specimen with or without an annular crack in its center. In the latter case, the crack is considered to initiate from a spherical pore and different radii of pore and crack have been tested. Fig. 4 shows the corresponding meshes, second order elements with a minimal size of 0.2 mm $*$ 0.2 mm at mid-height along the symmetry axis and a progressive enlargement towards the upper/lower face and the outer surface, where the element size was 1 mm $*$ 1 mm. The convergence of the computed stress, strain and damage fields as a function of the degree of mesh refinement was investigated and the above-mentioned element sizes were found to be quite sufficient. The evolution of stresses has been analyzed in detail at four locations, labeled A, B, C, and D in Fig. 4(a). Point A is near the upper edge, point B is deeper in the specimen, point C is at mid-height and mid radius, while point D is at the center of the specimen.

The numerical integration of the transient heat equation, starting from an initial uniform temperature between −20

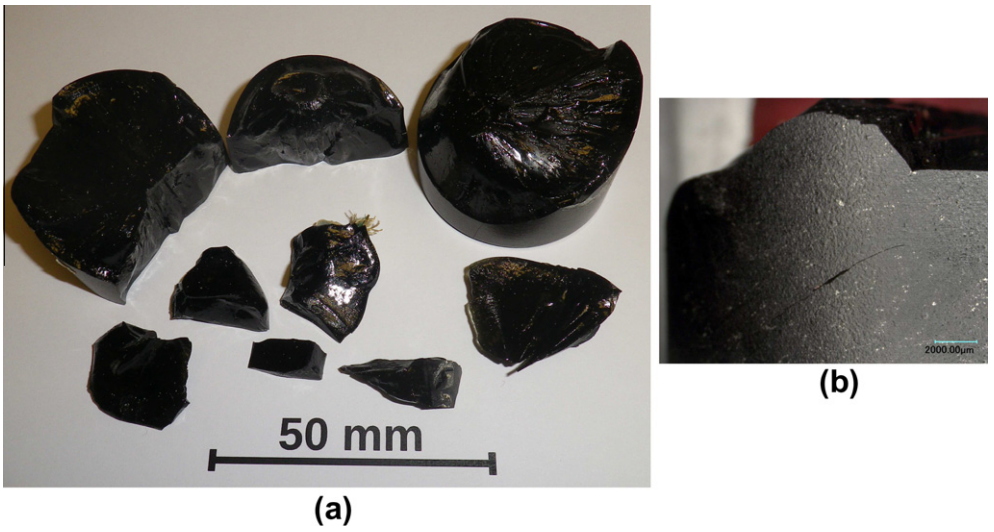

Fig. 2. (a) Fragments of a specimen broken by a severe thermal shock, (b) fragment containing arrested cracks.

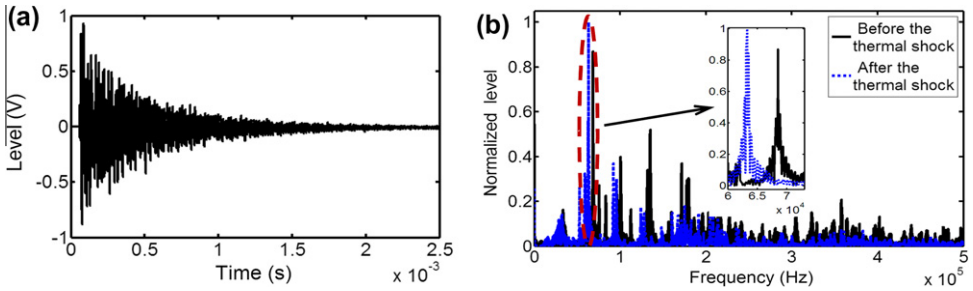

Fig. 3. Detection of internal damage in cylindrical specimens from vibration mode analysis. (a) Response to an impulse excitation. (b) Comparison of the amplitude spectra before and after thermal shock.

and −10 °C was split in two steps: (i) convective heating by ambient air during the time needed to take a specimen out of the freezer and prepare it for oil quenching and (ii) oil quenching, with imposed surface temperature, based on the thermal evolutions recorded by the thermocouples.

To model the 5 min of specimen preparation, convective heat transfer with ambient air at 20 °C was imposed along the external boundaries with a fixed convection coefficient. The natural convection coefficient in air is known to vary in the range 5–25 $Wm^2\,K^{-1}$. Simulations were thus done for 5, 10 and 25 $Wm^2\,K^{-1}$ and the final surface temperatures computed with 10 $Wm^2\,K^{-1}$ were found to be the closest to the measured surface temperatures just before oil quenching. This value of the convection coefficient was thus adopted.

It turned out that this period has a very limited influence on the temperature field: the surface temperature increases by 3 to 5 °C at most, while the temperature in the center remains unchanged.

To model the quenching stage, the temperature evolutions measured by the thermocouples glued on the upper and lower face were imposed along these faces, while the temperature measured by the thermocouple at mid-height was imposed there. For the other points along the side surface, a linear spatial interpolation between the three signals was made.

This surface temperature field was used as an input for the mechanical computation. The material was considered either as linear thermo-elastic, with temperature dependent properties, as detailed in Dube et al. (2010), or as thermo-elastic-damaging, using a modified version of the model introduced by Sun and Khaleel (2004). The nature of these modifications are detailed and discussed in a separate paper (Barth et al., 2013).

The stiffness degradation arising from damage is simulated by adding a damage-dependent (negative) term to the initial stiffness tensor in the thermo-elastic constitutive equation:

$$\sigma_{ij} = \left\{K^e_{ijkl}(T) + K^d_{ijkl}(T)\right\} \cdot \left\{\varepsilon_{kl} - \varepsilon^{th}_{kl}\right\} \tag{1}$$

Here σ_{ij} and ε_{kl} denote the stress and strain components, $K^e(T)$ and $K^d(T)$ are temperature-dependent fourth-order tensors corresponding respectively to the stiffness of the intact isotropic material and to the damage-induced degradation in stiffness. ε^{th}_{kl} denote thermal strain components. The initial and damage-related stiffness tensors are given respectively by:

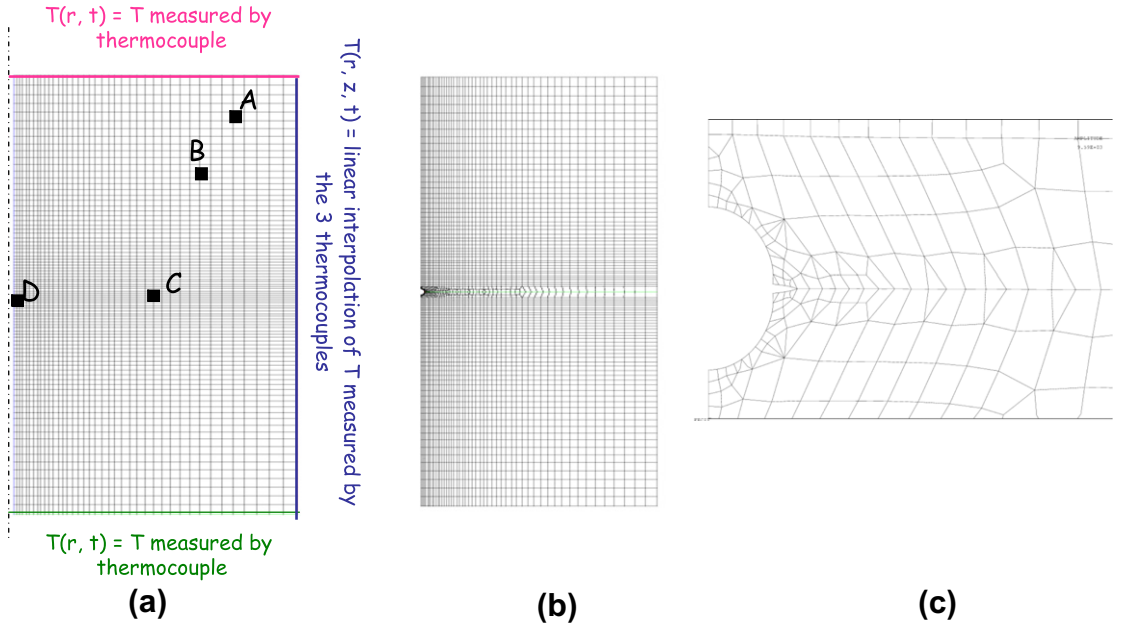

Fig. 4. (a) Axisymmetric F.E. model used to simulate the thermal shocks, (b) cylinder with an annular crack initiated from a spherical pore, (c) detail.

$$K^e_{ijkl} = \lambda(T)\delta_{ij}\delta_{kl} + \mu(T)(\delta_{ik}\delta_{jl} + \delta_{il}\delta_{kj}) \tag{2}$$

$$K^d_{ijkl} = C_1(T)(\delta_{ij}D_{kl} + \delta_{kl}D_{ij}) + \frac{1}{2}C_2(T)(\delta_{jk}D_{il} + \delta_{il}D_{jk} + \delta_{ik}D_{jl} + \delta_{jl}D_{ik}) \tag{3}$$

where $\lambda(T)$ and $\mu(T)$ denote Lamé's constants, D_{ij} the damage parameters and where $C_1(T)$ and $C_2(T)$ are two constants of the material. In principle, C_1 and C_2 are temperature-dependent, but a previous study (Dube et al., 2010) has shown that this temperature-dependence can be neglected up to 500 °C in this material. The components of the damage tensor, D_{ij}, are functions of the stress state and take values between zero and one, corresponding respectively to an intact or fully damaged material, i.e., which can no longer sustain stresses in the corresponding direction. Though the original damage model of Sun and Khaleel (2004) takes into account both shear and tension-induced damage, only the latter is considered here. Tensile damage is represented by the diagonal components of tensor D, which are assumed to grow with the applied stress as follows:

$$D_{ii} = \begin{cases} 0 & \sigma_i \leqslant \sigma_{th} \\ \frac{\sigma_i - \sigma_{th}(T)}{\sigma_c(T) - \sigma_{th}(T)} & \sigma_{th} < \sigma_i < \sigma_c \\ 1 & \sigma_i \geqslant \sigma_c \end{cases} \quad i = 1,2,3 \tag{4}$$

where, σ_i is the ith principal tensile stress, σ_{th} is the temperature-dependent threshold stress under which no damage occurs and σ_c is the temperature-dependent critical stress above which the material is fully damaged. In practice, for borosilicate glass, both σ_{th} and σ_c were found to be nearly independent of temperature up to 500 °C (Dube et al., 2010).

It is important to notice that these constitutive equations are formulated in the principal coordinate system and cannot be used easily if the principal axes turn. However, during "cold-to-hot" thermal shocks, loading was found to be strictly proportional only in the central part of the specimens, where damage concentrates and where the principal axes coincide with the (r,θ,z) axes. The constitutive equations were thus written in this cylindrical coordinate system, keeping in mind the fact that near the edges of the specimens, where the principal axes are different and vary in time, the model is not able to capture damage as well. From Eqs. (1)–(3), the glass constitutive equation expressed in cylindrical coordinates (r,θ,z) becomes:

$$\begin{Bmatrix} \sigma_{rr} \\ \sigma_{\theta\theta} \\ \sigma_{zz} \\ \sigma_{\theta zz} \\ \sigma_{rz} \\ \sigma_{r\theta} \end{Bmatrix} = \begin{Bmatrix} \lambda+2\mu+2D_{rr}(C_1+C_2) & \lambda+C_1(D_{rr}+D_{\theta\theta}) & \lambda+C_1(D_{rr}+D_{zz}) & 0 & 0 & 0 \\ \lambda+C_1(D_{rr}+D_{\theta\theta}) & \lambda+2\mu+2D_{\theta\theta}(C_1+C_2) & \lambda+C_1(D_{\theta\theta}+D_{zz}) & 0 & 0 & 0 \\ \lambda+C_1(D_{rr}+D_{zz}) & \lambda+C_1(D_{\theta\theta}+D_{zz}) & \lambda+2\mu+2D_{zz}(C_1+C_2) & 0 & 0 & 0 \\ 0 & 0 & 0 & \mu+\frac{C_2(D_{zz}+D_{\theta\theta})}{2} & 0 & 0 \\ 0 & 0 & 0 & 0 & \mu+\frac{C_2(D_{rr}+D_{zz})}{2} & 0 \\ 0 & 0 & 0 & 0 & 0 & \mu+\frac{C_2(D_{rr}+D_{\theta\theta})}{2} \end{Bmatrix} \begin{Bmatrix} \varepsilon_{rr} \\ \varepsilon_{\theta\theta} \\ \varepsilon_{zz} \\ 2\varepsilon_{z\theta} \\ 2\varepsilon_{rz} \\ 2\varepsilon_{r\theta} \end{Bmatrix} \tag{5}$$

Since the model was applied to "cold-to-hot" thermal shocks that induce, as shown below, a nearly equi-triaxial tension at the critical point, the values of C_1 and C_2 were chosen so that the stresses σ_{rr}, $\sigma_{\theta\theta}$, σ_{zz}, $\sigma_{\theta z}$, σ_{rz} and $\sigma_{r\theta}$ all fall to zero when $D_{11} = D_{22} = D_{33} = 1$, for equi-triaxial tension. In such a loading case, all principal strains are equal: $\varepsilon_{11} = \varepsilon_{22} = \varepsilon_{33} = \varepsilon$ and two conditions have to be satisfied:

$$\sigma_{rr} = \sigma_{\theta\theta} = \sigma_{zz} = \{\lambda + 2\mu + 2(C_1 + C_2)\}\varepsilon + 2\{\lambda + 2C_1\}\varepsilon = 0 \quad (6)$$

$$\sigma_{rz} = \sigma_{r\theta} = \sigma_{\theta z} = (\mu + C_2)\varepsilon = 0 \quad (7)$$

It follows that $C_1 = -0.5\,\mu$ and $C_2 = -\mu$.

The constitutive law was programmed in the object-oriented finite element language of *Cast3m* (http://www-cast3m.cea.fr/). The time stepping algorithm follows a forward integration scheme, in which n and $(n-1)$ denote the nth and $(n-1)$th time step of the analysis, respectively. The analysis is conducted incrementally, i.e., the stresses are computed at each step as:

$$\sigma_{ij}^{n} = \left\{K_{ijkl}^{e} + K_{ijkl}^{d,(n-1)}\right\} \cdot \left\{\varepsilon_{kl}^{n} - \varepsilon_{kl}^{th,n}\right\} \quad (8)$$

where the stiffness tensor accounting for damage is calculated based on the stresses of the previous time increment.

Since the specimens are initially considered flawless, the damage parameters are set to zero at the beginning of the analysis. Since all points eventually experience unloading, it is necessary to check at each time step that D_{ii} does not decrease (damage is irreversible):

$$D_{ii} = \max\left(D_{ii}^{n}, D_{ii}^{n-1}\right) \quad (9)$$

The vibration eigenfrequencies of the specimens were computed before and after the simulation of the thermal shocks, using the mesh shown in Fig. 3(a). In the latter case, it was the final stiffness tensor obtained at the last time step of the thermal shock simulation which was retained. The eigenvectors and eigenvalues of:

$$K - \varpi^2 M = 0 \quad (10)$$

where K is the stiffness matrix and M is the mass matrix where searched in the following basis (axisymmetric solutions correspond to $k = 0$):

$$u(r,\theta,z,t) = \sum_{k=0}^{n} u(r,z,t).\cos(k\theta) \quad (11)$$

In practice, with n equal to 15, most of the resonance frequencies measured on intact specimens were found by F.E. computations.

One of the main observations was that pores play a prominent role in fracture. Therefore, various analyses were done on a sub-model including an isolated pore or a pore surrounded by one or several orthogonal annular

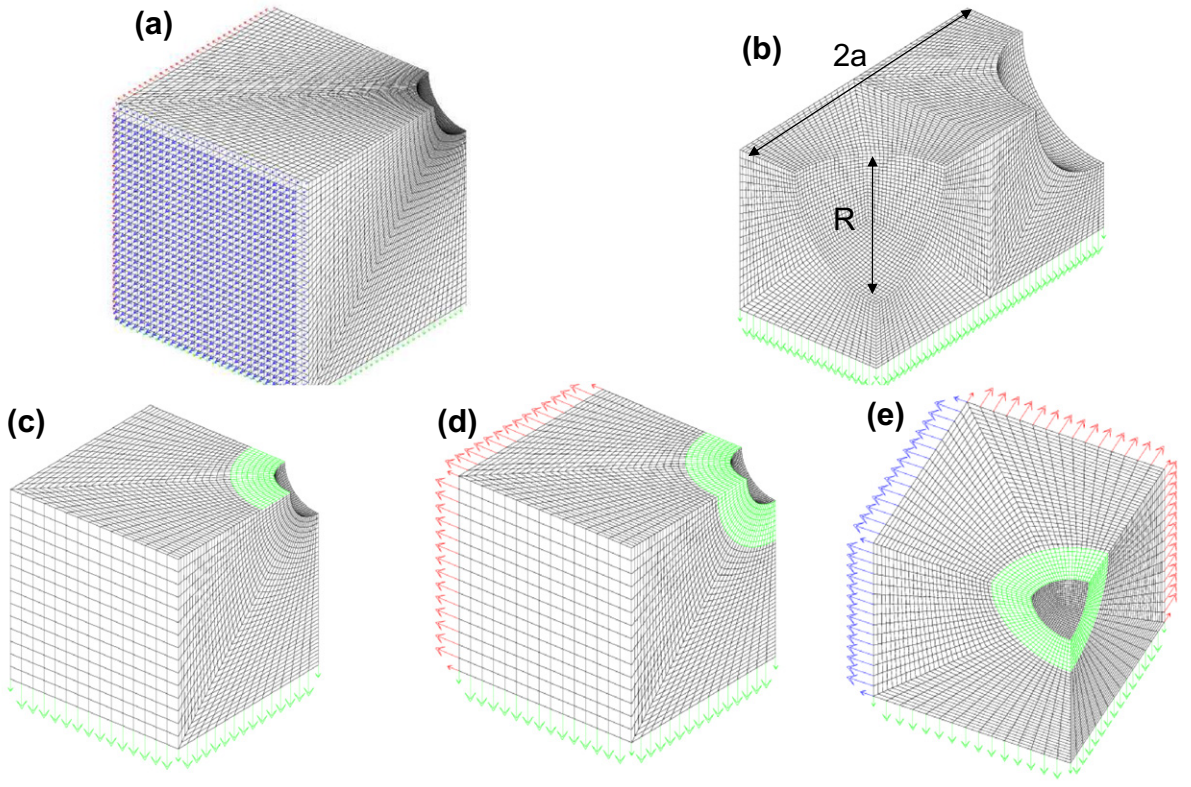

Fig. 5. Models used to compute (a) and (b) the stress concentration near a single or two spherical pore(s) or (c) K_I along the front of an annular crack initiated from a pore under uniaxial, biaxial or triaxial tension (c), (d) K_I along the front of two (resp. three) orthogonal cracks initiated from a pore under biaxial (resp. triaxial) tension.

cracks (see Fig. 5) and submitted to a triaxial loading extracted from the previous cylindrical model, in order to evaluate the stress concentration in the first case and stress intensity factors in the latter.

The finite element models shown on Fig. 5(a)–(c) respectively, represent one eighth of a pore embedded in a cubic matrix with or without the annular cracks. The half-length of the matrix was five times the radius of the hole. Symmetry boundary conditions were enforced on the three faces that cut the pore and uniform normal stresses applied on one, two or three other faces, as illustrated by the colored arrows. The stresses near the pore surface on the three main planes were extracted and the stress concentration was deduced. The mode I stress intensity factors were computed using the G-theta method (Destuynder et al., 1981).

The meshes shown on Fig. 5(d) and (e) were used to analyse the interactions between two or three mutually orthogonal annular cracks of similar size initiated near the same pore under equibiaxial or equitriaxial tension, respectively.

3. Experimental results and thermoelastic numerical analysis

3.1. Preliminary computations assuming a linear thermoelastic behavior

Fig. 6 shows the contours of the first principal stress at four different moments of a thermal shock with $\Delta T = 294\,^{\circ}C$. A weak tensile peak first appears near the edges of the specimen at 45° with respect to the symmetry axis of the cylinder. The tension peak is then progressively shifted towards the inside of the specimen, while its value increases. Finally it reaches its maximum value at mid-height, on the symmetry axis.

The evolutions of the three principal stresses have been computed at points A, B, C and D (see Fig. 1(a)) and are plotted in Fig. 7.

Peak stresses occur earlier near a free surface, where loading is non-proportional, but are smaller than at points located deeper inside. Near the center-point (labeled D), loading is proportional and the principal directions are r, θ and z. The stress state and triaxiality are quite different from one place to another. Only one principal stress is always positive at point A, two at point B, while points C and D experience triaxial tension during the whole test. The stress concentration near the pores thus varies, according to their position in the specimen, as shown below.

Let us first recall that Goodier (1933) provided analytical expressions of the stresses near a spherical pore in an elastic infinite medium under uniform loading. For a Poisson's ratio $\nu = 0.245$, the stress concentration factor near a pore is 2.02, 1.44 and 1.38 for uniaxial, equibiaxial and equitriaxial tension, respectively. But these expressions cannot be used for pores located near the edges of finite size specimens or in areas where stress gradients exist.

The stress concentration near pores potentially located at points A, B, C, and D in the specimens was thus evaluated numerically, by applying the three principal stresses (computed in homogeneous flawless glass at the moment corresponding to the peak value of the first principal stress) on the boundaries of the F.E. model shown in Fig. 2(a).

Fig. 8 compares the time evolution of the first principal stress at A, B, C, and D. The stress concentration factor K_t induced by a pore at each point is also indicated, as well as the resulting local stress (K_t times the peak value of the first principal stress).

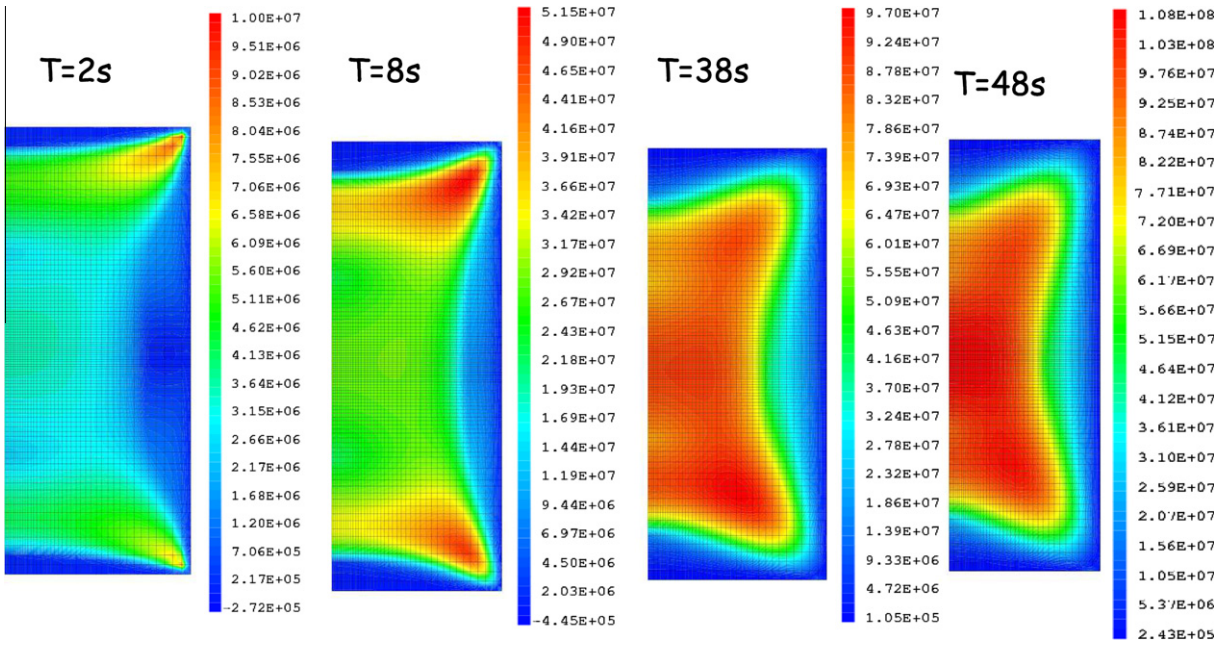

Fig. 6. Contours of the first principal stress at various moments of a thermal shock.

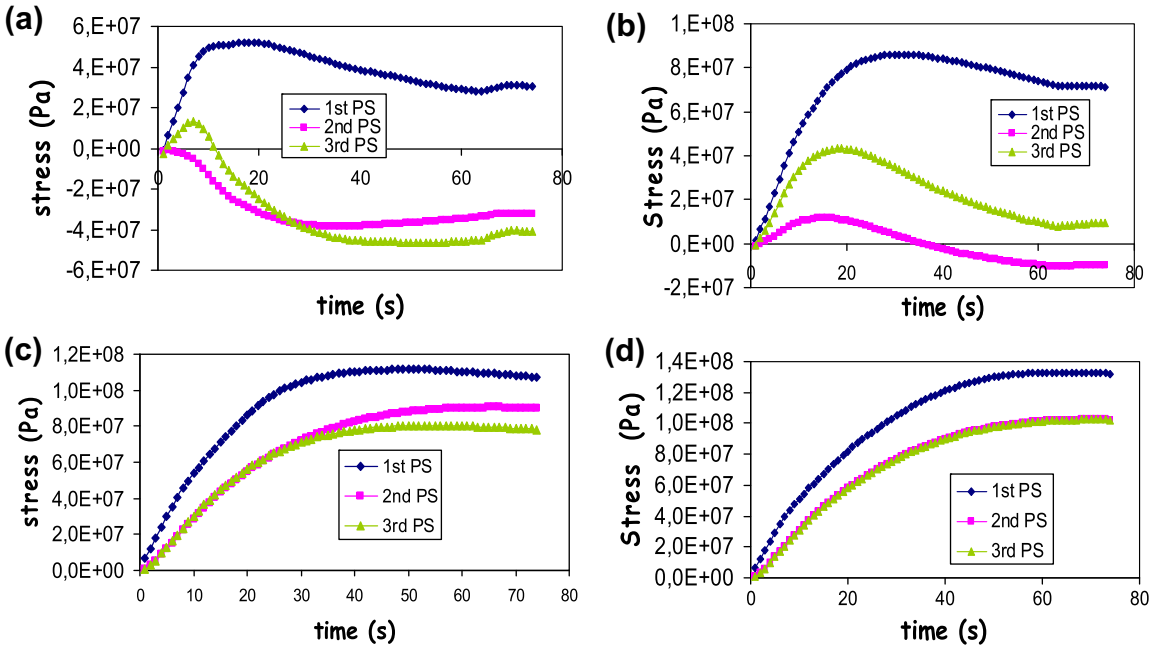

Fig. 7. Evolution of principal stresses at points A, B, C, D during test 5.

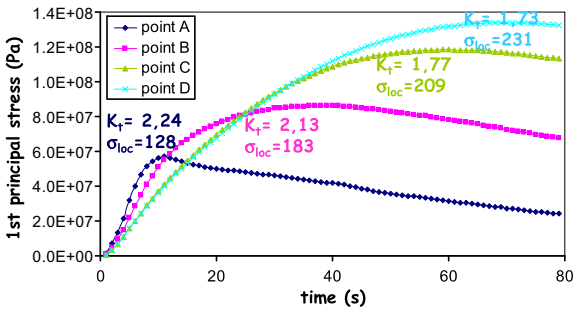

Fig. 8. Compared evolution of the first principal stress and of K_t at points A, B, C, D.

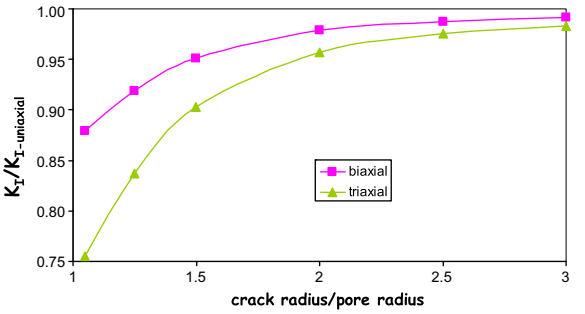

Fig. 9. Influence of triaxiality on K_I for an annular crack initiated at a pore.

K_t was found to decrease from 2.24 to 2.13, 1.77 and finally 1.73, going from point A to point D. Pores should thus be less detrimental under triaxial than uniaxial loading.

This conclusion is also supported by the comparison of the stress intensity factors computed for an annular crack initiated from a pore under uniaxial, biaxial or triaxial tension (Fig. 9). When the radius of the crack is less than 2.5 to 3 times that of the pore, biaxial loading substantially reduces the crack driving force compared to uniaxial loading. This reduction is enhanced when triaxial loading is applied. However, this effect tends to vanish when the crack grows away from the pore, since non-singular T-stresses do not affect K_I in a homogeneous medium.

Moreover, several orthogonal cracks might initiate around a given pore under multiaxial loadings. Finite element computations of K_I have been made along the front of two cracks under equi-biaxial tension and three cracks under equi-triaxial loading. The values found at the intersection points where corner-point singularities prevail were discarded. A shielding effect was found: under biaxial tension, the presence of a second cracks, reduces the mean K_I by a factor of 0.89, while the presence of a third crack under triaxial tension reduces K_I by a factor of 0.80.

If the potential presence of a pore at A, B, C, or D is taken into account, the local amplified stress is still predicted to increase from 128 to 183, 209 and finally 231 MPa (Fig. 7). Damage initiation, is thus expected near the center of the cylinders, if the pores can be considered as isolated.

For fixed thermal boundary conditions, varying the height of the specimens changes the stress state in the critical area, as illustrated in Fig. 7. For short specimens ($H < 36$ mm), the radial and hoop stresses are predominant in the center when compared to the axial component (Fig. 10(a)) and vice versa for high specimens (Fig. 10(b)). "Cold to hot" thermal shocks on cylinders thus constitute a convenient way to apply triaxial tension to a brittle material. Moreover, the desired proportion of axial, radial and tangential stresses can be achieved by a simple adjust-

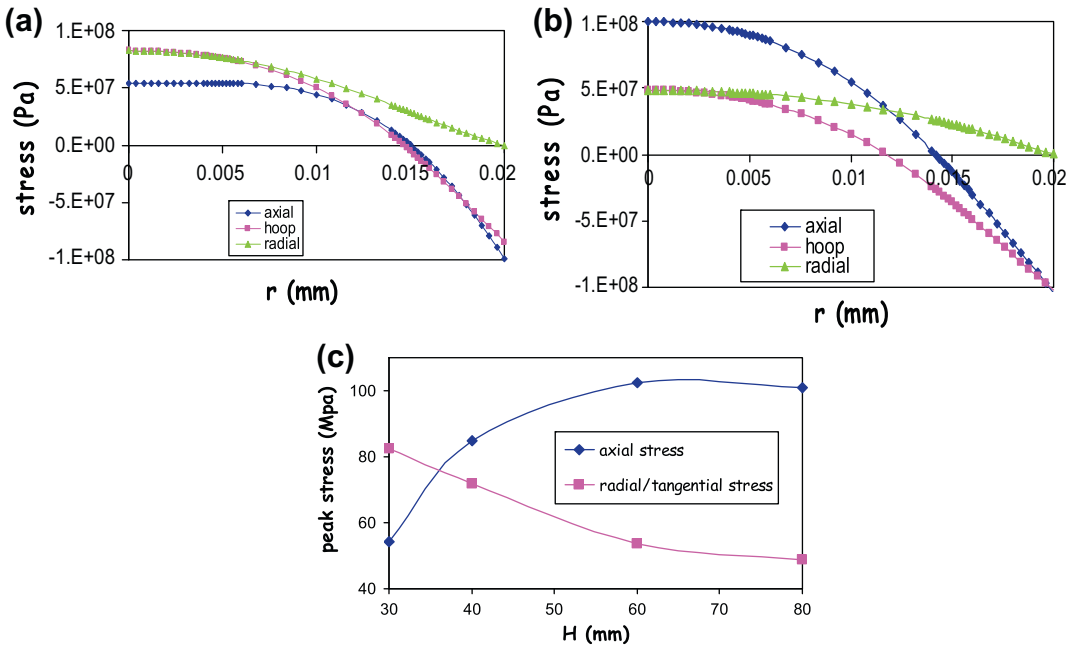

Fig. 10. Radial stress profiles at mid-height for (a) $H = 30$ mm and (b) $H = 80$ mm. (c) Peak stresses as a function of H.

ment of the height-to-diameter ratio of the specimens (Fig. 10(c)).

3.2. Experimental results and discussion

The conditions and basic results of the thermal shocks are summarized in Table 1 where the height of the specimens, the amplitude of the thermal shock and the peak value of the first principal stress at the center-point, D for unbroken specimens are indicated.

The specimens in the first four columns did neither fracture, nor emit any noise during quenching. Careful observations of polished longitudinal and transverse sections did not reveal any damage. The analysis of the vibration spectra measured after the thermal shocks did not show any significant shift in eigenfrequencies (Fig. 11).

By contrast, a decrease in eigenfrequencies ranging from 1 to 6 kHz, depending on the mode was observed in specimen $n°7$ (Fig. 11), in which some internal microcracks were observed. These microcracks have an approximatively radial orientation and are located within 4.5 mm from the specimen axis, on transverse sections at mid-height (Fig. 12).

Fig. 13 illustrates the typical aspect of broken specimens, characterized by a 3D star-like crack pattern, with

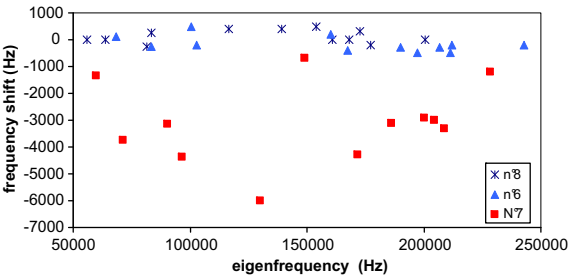

Fig. 11. Measured shifts in eigen-frequencies for three specimens.

a typical "mirror, mist and hackles" pattern at mid-height along the symmetry axis at the initiation site. The mirror zone surrounded a pore responsible for crack initiation. Beyond this flat penny-shaped zone, crack branching occurred into a large number of tilted and twisted parts, visible in transverse and longitudinal sections (Fig. 13(c) and (d), respectively). Note that the bifurcation point does not coincide with the change from a predominant axial stress to a predominant tangential or radial stress, which occurs for a much larger radius (see Fig. 10(b)). Fracture in specimen 5 occurred from two crack initiation sites. A pore gave rise to a penny-shape crack (Fig. 13(b)) oriented

Table 1
Results of thermal shock experiments.

Test $n°$	12	6	8	7	10	0	9	5	11	4
H (mm)	45	36.6	45	40.5	45	48.5	45	45	45	44.6
ΔT (°c)	286	314	291	323	301	314	320	344	296	342
Observed damage	None			Micro cracks	Fracture from the bulk				Edge scaling from pore clusters	
Peak P.S. at D Mpa	90	90.5	97.1	99.4						

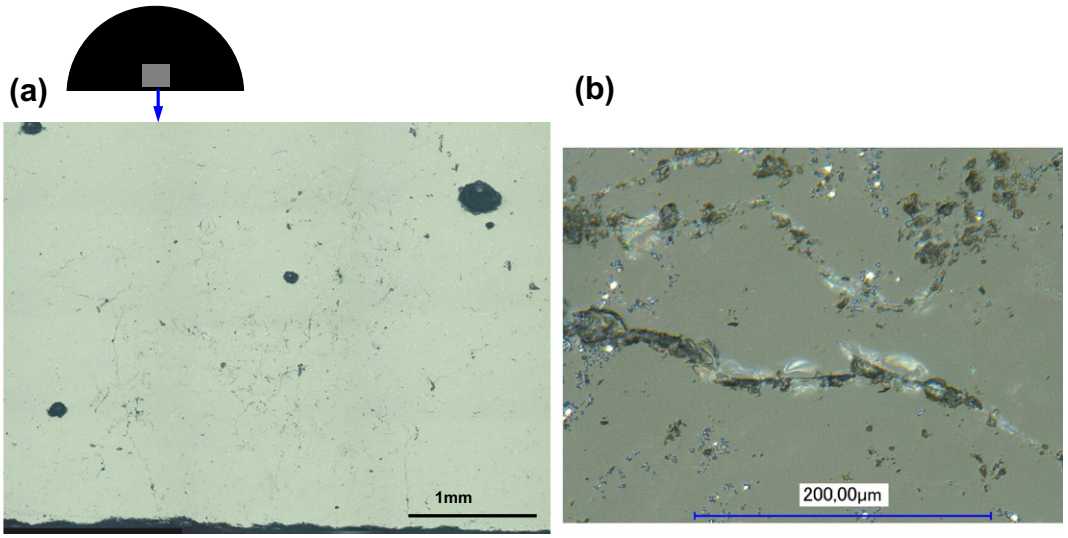

Fig. 12. Microcracks on a transverse section of specimen $n°7$, at mid-height. (a) Global view of a $4.18 * 4.5$ mm-wide central zone, (b) detail.

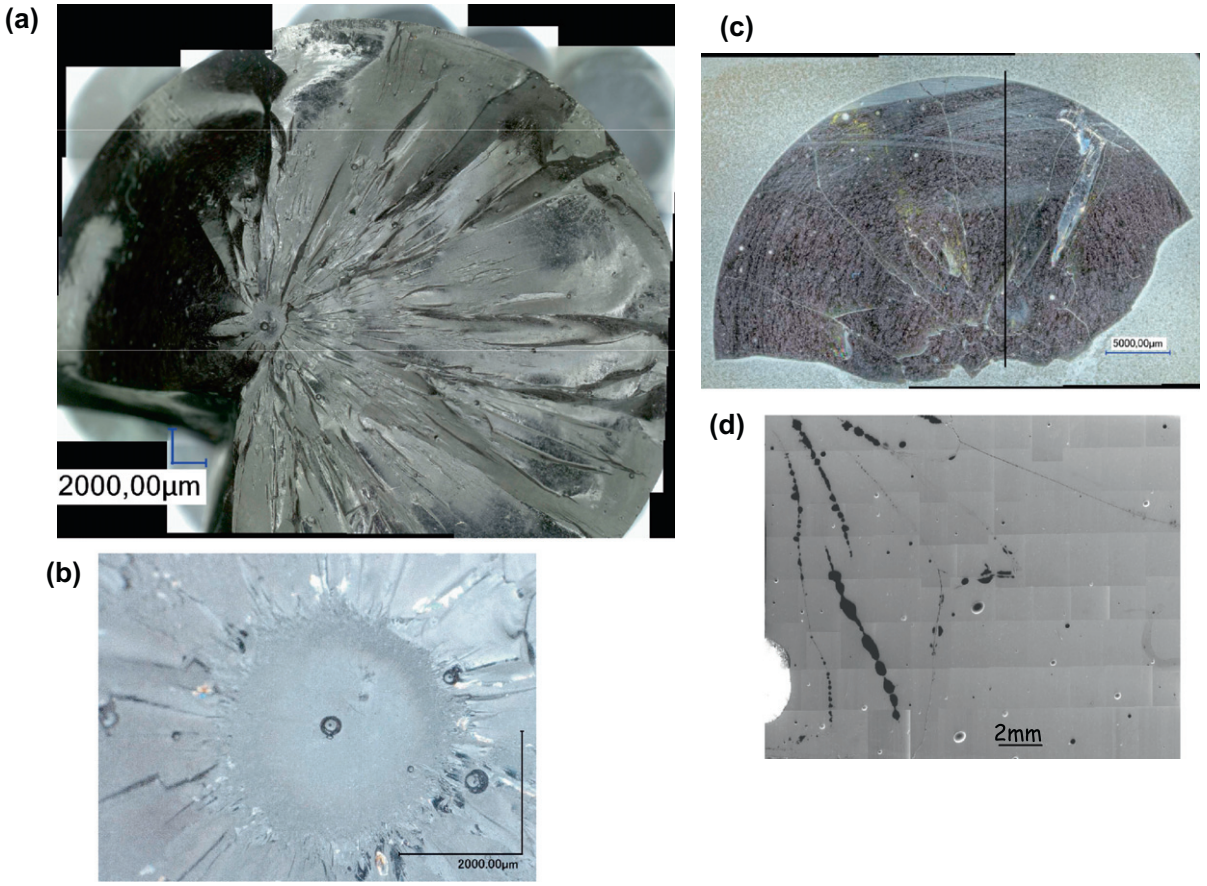

Fig. 13. Fractured specimen (a) typical global aspect, (b) mirror zone, (c) transverse section (d) longitudinal section along the line drawn in (c).

35° away from the axis. A more or less circular "mirror zone" with a similar diameter, almost normal to the axis, but somewhat shifted from the center and from the mid-height plane, was also observed.

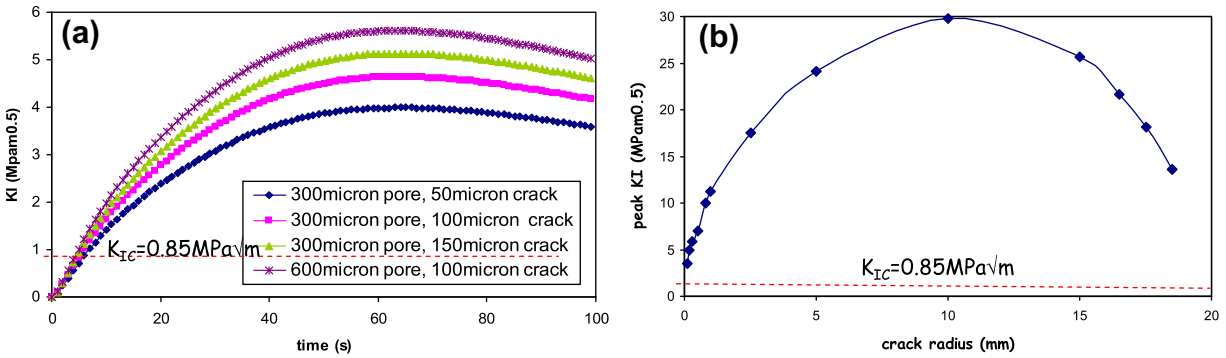

Fig. 14. (a) K_I for a crack initiated from a pore, at mid-height of a cylinder, for test $n°4$, (b) peak value of K_I as a function of the crack length.

Table 2
Coordinates (in a referential centered at mid-height), size and stress at the center of the fracture mirrors. Stress concentration factor due to the presence of a pore and amplified stress.

Test $n°$	r (mm)	z (mm)	R_m (mm)	t_f (s)	σ_f (MPa)	K_t	$K*\sigma_f$ (MPa)
0	5.96	0.45	1.258	112	92	1.83	168.2
5	4.67	10.57	1.835	65	77	1.82	140
5	10.18	11.24	1.835	65	69.3	2.12	147.1
9	10.0	5.29	4.42	19	54.6	1.82	99.6
10	11.1	1.67	3.2	39	62.2	1.82	113.4

The reasons for the transition from the mirror (a single, penny-shape crack) to the mist and then hackles pattern have been discussed by many authors (Yoffe, 1951; Sharon and Fineberg, 1999a,b; Cramer et al., 2000; Rabinovitch and Bahat, 2008) and lie in the dynamic character of crack growth in brittle materials. At high crack growth rate, a plateau in the angular distribution of the hoop stress $\sigma_{\theta\theta}(r,\theta)$ ahead of the tip appears, instead of a clear maximum at 0° as for a stationary crack, so that crack growth in a wider and wider angular range becomes possible as the crack accelerates. Above a given crack growth rate, the maximum $\sigma_{\theta\theta}(r,\theta)$ even switches to a finite, growth-rate-dependent angle, this finally inducing bifurcation (Yoffe, 1951). In glass, above a crack growth rate around 1500 m/s, Sharon and Fineberg (1999b) observed that micro-branches of increasing size repeatedly nucleate and abort (this producing the "mist" region), inducing some oscillations in the growth rate of the main crack around a stable value. Near this "terminal velocity" (a fraction of the celerity of Rayleigh) the rate of energy dissipation by the acceleration of a single crack is insufficient and segmentation into many cracks is more efficient in terms of energy dissipation.

To check whether such dynamic crack growth is effectively likely to occur during our thermal shock experiments, the stress intensity factor for a stationary crack initiated from a pore, at mid-height of a cylinder, during such a thermal shock (test $n°4$) was computed for various pore sizes and various crack lengths. The results are plotted as a function of time on Fig. 14(a). Fig. 14(b) shows the peak value of K_I as a function of the total crack radius.

Very early and for very small cracks K_I exceeds K_{Ic} ($0.85\ \mathrm{MPa}\sqrt{\mathrm{m}}$) and the crack driving force keeps on increasing in time, reaching 5 to 8 times K_{Ic} so that a sharp acceleration should occur. The peak value of K_I also increases with the crack radius, until it reaches 10 mm. Dynamic effects can indeed be expected and fracture is probably controlled by crack initiation, all around a pore, rather than by crack growth.

An additional reason for the observed tilting and twisting of the crack can also be invoked: due to the triaxial tension in the specimen, the crack experiences two positive T-stresses: σ_{rr} parallel to its front and $\sigma_{\theta\theta}$ tangent to the front. Such positive non-singular stresses are known to make the straight crack path unstable (Cotterell and Rice, 1980). The former should favor crack tilting and the latter crack twisting.

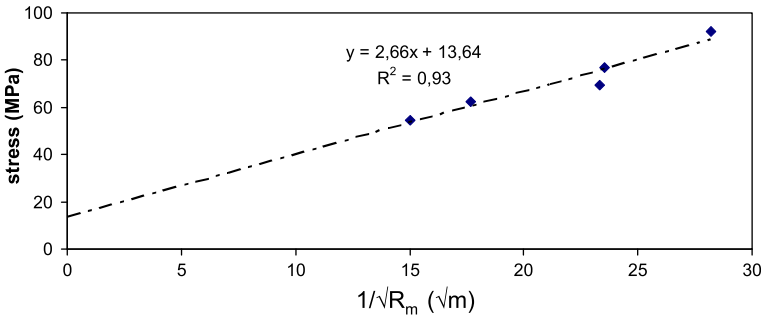

Fig. 15. Analysis of fracture mirrors size.

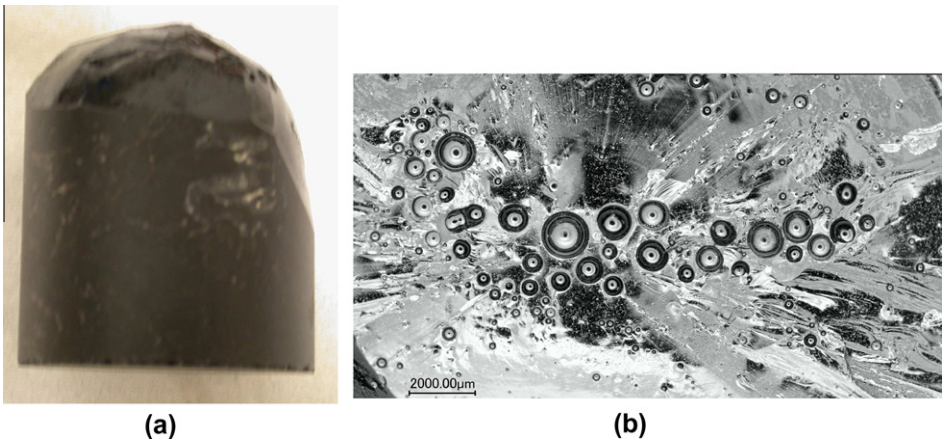

Fig. 16. Scaled specimen 11 (a) side view, (b) pores cluster at the origin of scaling.

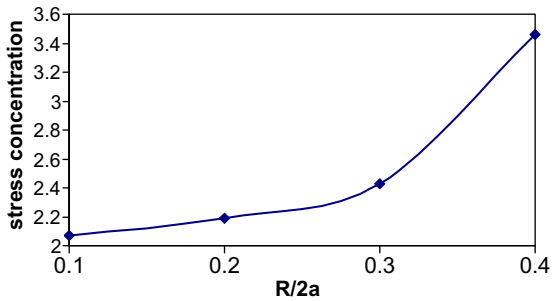

Fig. 17. Evolution of the stress concentration factor near a spherical pore with the normalized distance to a neighboring identical pore, under uniaxial tension.

The measurement of fracture mirror sizes is considered by Mecholsky (1995) and others (Shi et al., 1989; Quinn, 1999) as a reliable tool to evaluate the stress at fracture, σ_f, in a brittle material, since an empirical relationship between the latter and the radius of the mirror-mist boundary has been established based on a large number of experiments:

$$\sigma_f \sqrt{R_m} = A \tag{12}$$

where A, the "mirror constant" is characteristic of the material, independent of the test environment (Quinn, 1999) and, in the case of borosilicate glass, independent of temperature, at least in the range −150 °C – 85 °C (Shi et al., 1989). Quinn (1999) used various test conditions to obtain a large range of mirror sizes in a crown borosilicate

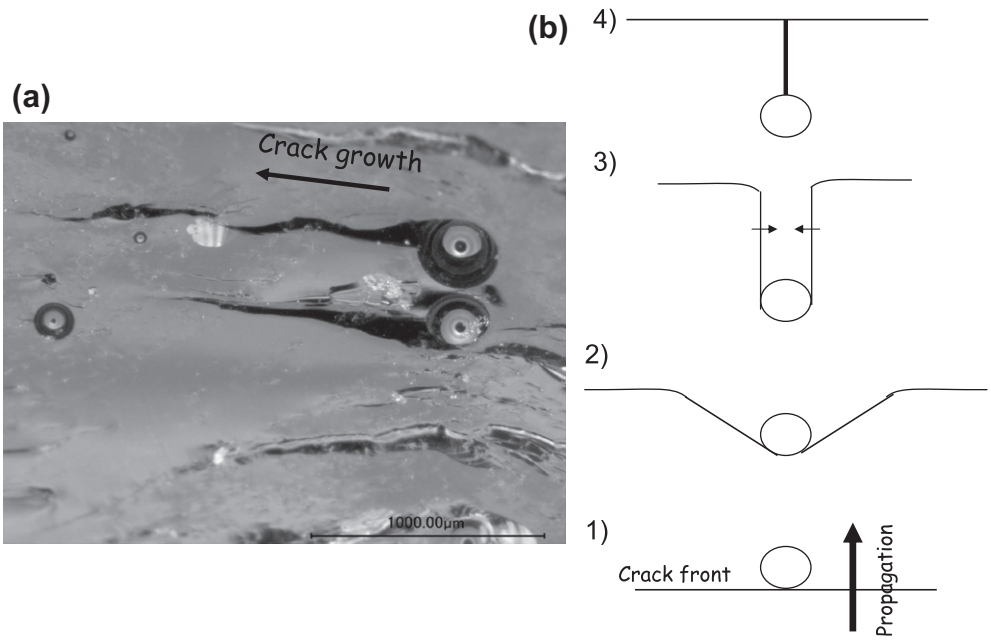

Fig. 18. (a) Secondary longitudinal cracks on pores cut by a main crack, (b) possible scenario for their formation.

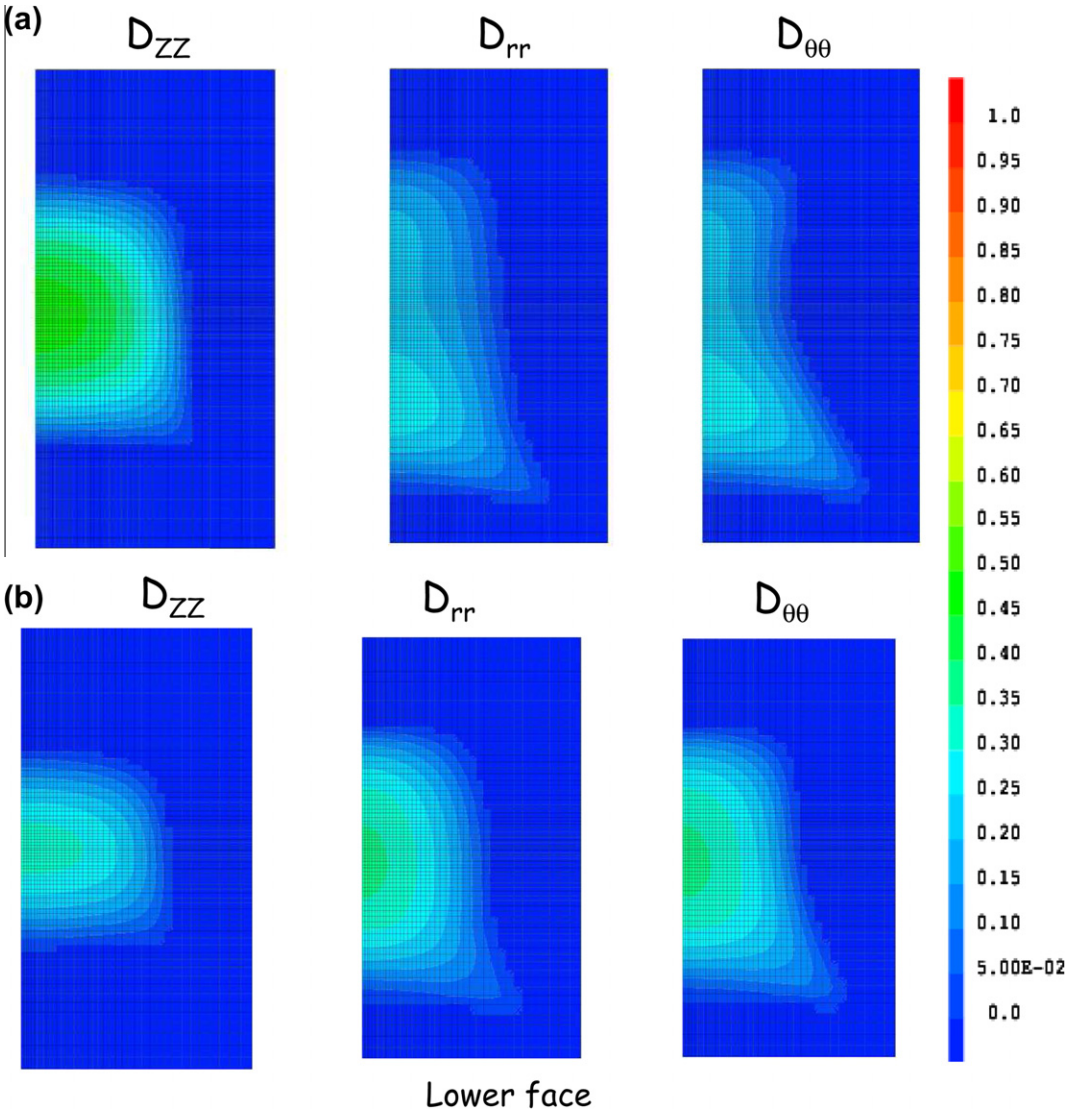

Fig. 19. Final contours of damage parameters predicted for $\sigma_{threshold}$ = 50 MPa, $\sigma_{critical}$ = 110 MPa with the thermal history of test 5 for two specimen heights: (a) H = 45 mm (b) H = 35 mm.

glass and observed that a modified version of Eq. (12) with a threshold stress, σ_t, fits better the data:

$$(\sigma_f - \sigma_t)\sqrt{R_m} = A \tag{13}$$

In the present study, the radius R_m of the mirrors and the coordinates (r,z) of their center in the cylindrical specimens were measured. Then the first principal stress at this position, at the instant of fracture t_f (easily determined by the emission of a loud noise) was computed by finite element. All those data are reported in Table 2.

Fig. 15 shows a plot of σ_f versus $1/\sqrt{R_m}$. Like in the work of Quinn (1999) the plot is linear, with a slope of 2.66 MPa$\sqrt{\text{m}}$, but does not intersect the origin. The y-intercept is 13.6 MPa, which thus corresponds to the threshold σ_t. Anyway, this good correlation of mirror sizes with the computed stress levels in various specimens, at various times at positions proves their consistency.

The stress concentration factors at the pores responsible for the nucleation of the mirror cracks were computed at the moment of fracture using the sub-modeling procedure described above and the results are reported in Table 2, as well as the effective, amplified local stress. In all cases, the latter is higher than the peak tensile stress computed at the center of non-damaged specimens (at most 97.1 MPa, see Table 1). This suggests that the latter did not undergo damage due to the absence of pore at the most critical point.

Scaling at nearly 45° to the axis, near the upper or lower edges occurred in some specimens. Fractographic observations (Fig. 16) revealed that pore clusters were responsible for this kind of damage. As expected, finite element computations using the mesh shown in Fig. 4(b) showed that

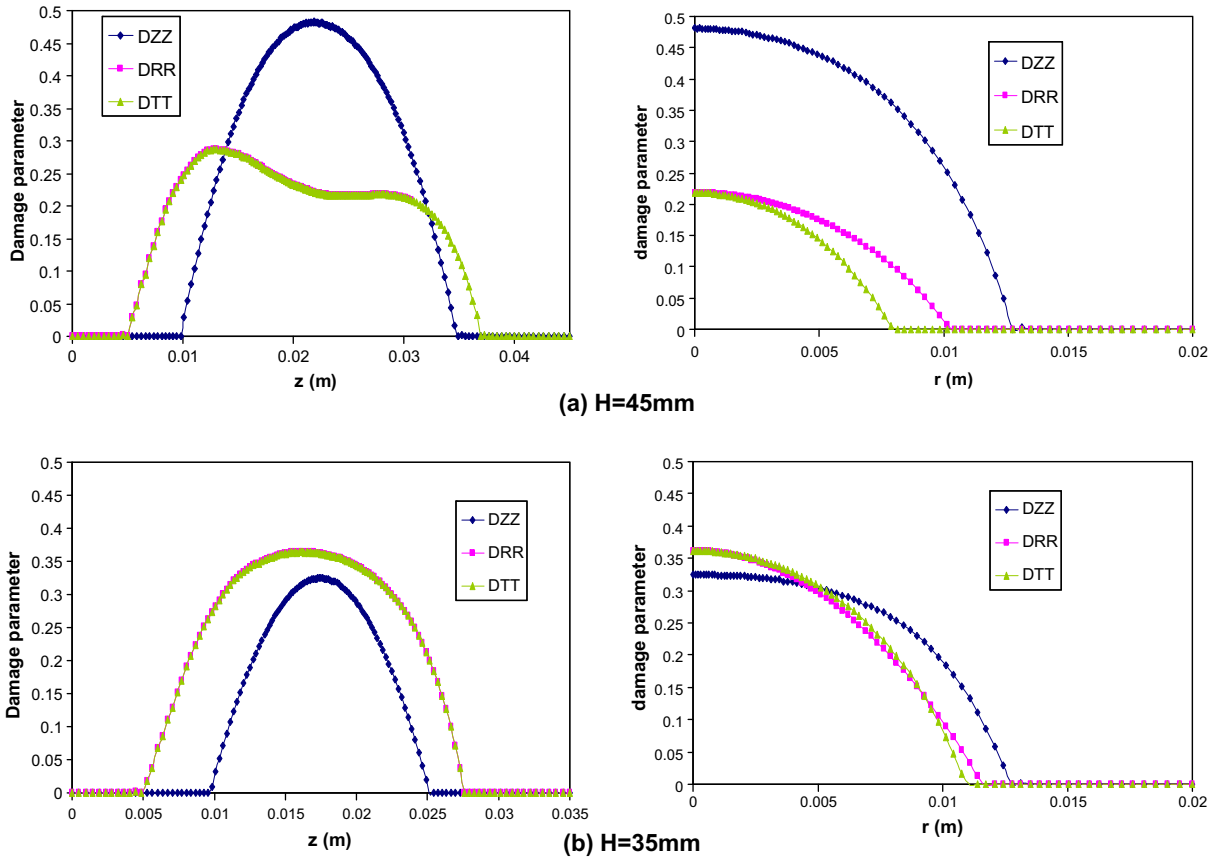

Fig. 20. Axial and radial profiles of damage parameters at mid-height predicted for $\sigma_{threshold}$ = 50 MPa, $\sigma_{critical}$ = 110 MPa with the thermal history of test 5 for two specimen heights: (a) H = 45 mm, (b) H = 35 mm.

the stress concentration in-between neighboring pores is higher than near an isolated pore and rises as the distance between the pore decreases (Fig. 17).

A recurrent pattern was observed on broken specimens: secondary longitudinal cracks on the "exit" side of pores cut by a propagating crack (Fig. 18(a)). A scenario (Fig. 18(b)) can be proposed to explain the systematic formation of such marks. When an initially straight crack front meets a pore (1), the part of the front tangent to the pore gets pinned, because it is locally blunted and the stress singularity vanishes there. But both sides of the front continue to propagate (2), so that the front adopts a U shape whose width more or less corresponds to the diameter of the pore (3). Finally, the interaction between the two branches of the U leads to their coalescence (4), but due a slight misalignment inducing some mode II, a small step is formed when the two sides of the crack front meet, leaving the observed marks.

An increase in the number of fragments was noticed as the thermal amplitude increased. A total developed fracture surface of 68.8 cm^2 was measured in specimen n°10 (ΔT = 301 °C) and 90.2 cm^2 for specimen n°9, (same height, ΔT = 320 °C). Such data can be compared, as shown below, to some predictions issued from F.E. computations of the elastic energy associated to transient stresses and strains, to be released by fracture, in the damaged area of the specimen.

4. Prediction of thermal-shock-induced damage

Due to the heterogeneity of the material in terms of pore distribution, it is difficult to identify a threshold stress and a critical stress for damage with a sufficient degree of confidence from the limited amount of data available at that stage. Tests have to be repeated in order to obtain statistically significant results and to be able to adjust parameters representative of the average behavior. In this part, numerical simulations run with arbitrary values ($\sigma_{threshold}$ = 55 MPa, $\sigma_{critical}$ = 110 MPa) are presented just to illustrate qualitatively the possibilities of the model.

Fig. 19 compares the final contours of the damage parameters predicted for the thermal history of test n°5 for two specimen heights: 45 mm and 35 mm. Fig. 20 compares their axial and radial profiles, at mid-height. Damage normal to the axis (represented by D_{zz}) is predicted to develop mainly from the center and to predominate in the 45 mm-high specimen. By contrast, the radial and tangential damages, which are predicted to predominate in the 35 mm-high specimen (as expected from the different stress state shown in figure) are more diffuse, and slightly

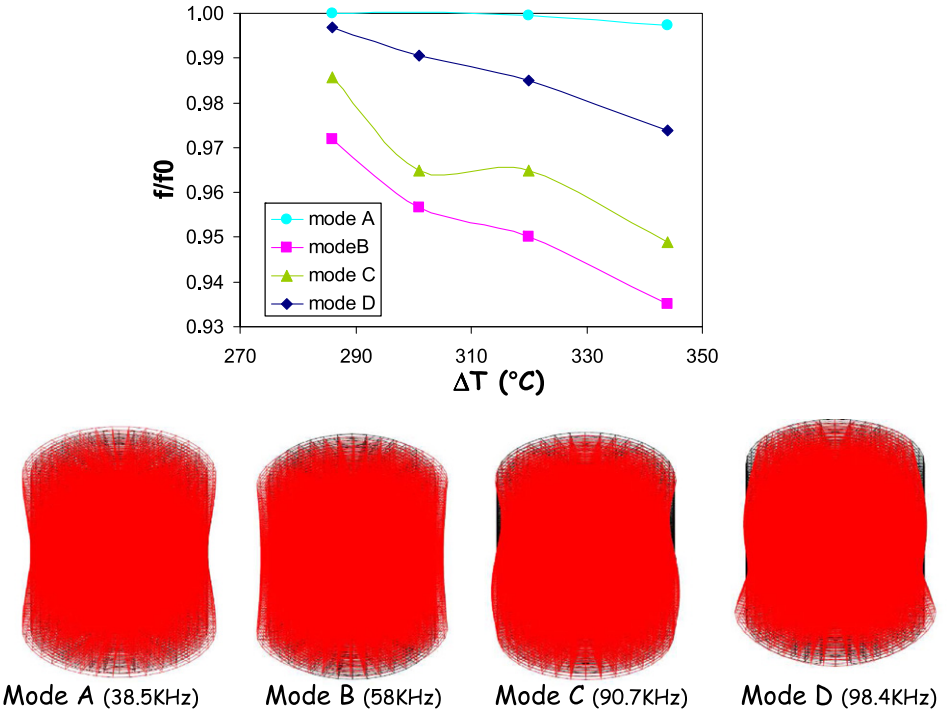

Fig. 21. Predicted evolution of three eigenfrequencies, with the corresponding deformed mesh (in red) superimposed on the undeformed mesh (in black). (For interpretation of the references to colour in this figure legend, the reader is referred to the web version of this article.)

shifted towards the face which enters first the oil bath. The positions of the center of the mirror zones which have been observed in specimen 5 and 0 are consistent with the predicted distribution of damage and their orientation as well: the mirrors found at small r values are normal to the axis.

The surface temperatures recorded by the thermocouples during tests 12a ($\Delta T = 286\,^{\circ}C$), 10 ($\Delta T = 301\,^{\circ}C$), 9 ($\Delta T = 320\,^{\circ}C$) and 5 ($\Delta T = 344\,^{\circ}C$) were used as boundary conditions for simulations of thermal shocks with $H = 45$ mm followed by computations of eigen-frequencies of the damaged specimens. Fig. 21 shows the predicted decrease of four of those frequencies (normalized by their initial values in intact specimens) as a function of the amplitude of the thermal shock. The corresponding deformed mesh, plotted in red is superimposed on the undeformed mesh, plotted in black. The higher the thermal amplitude, the more pronounced the drop in eigen-frequency. However, this drop varies substantially from mode to mode. In particular, mode A in which the mid-height area of the specimen -where damage tends to concentrate – does not move is weakly affected by the thermal shock, contrary to mode B for which the whole lateral surface moves laterally.

An upper bound has been obtained for the increase of the glass specimens surface due to thermal shock-induced cracking, assuming that all the dissipated energy, denoted by E_{dis} is consumed by the creation of new surfaces, which, according to Lemaître and Chaboche (1994) yields:

$$E_{dis} = -\int_0^t \int_V \varepsilon_{elas} \dot{K}^d \varepsilon_{elas} \cdot dV \cdot dt \approx \gamma_s S_{tot} \tag{14}$$

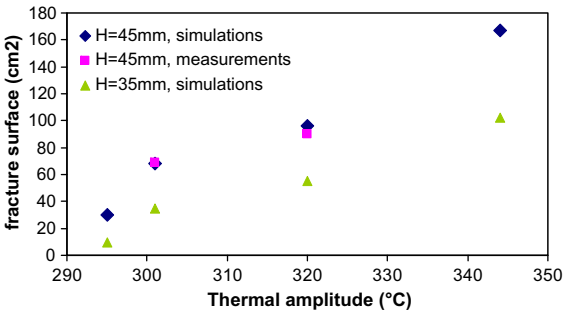

Fig. 22. Predicted fracture surface as a function of the amplitude of the thermal shock.

where S_{tot} denotes the cumulated surface of cracks and γ_s the surface energy. The latter is deduced from the toughness, K_{Ic}, by means of Griffith's equation:

$$\gamma_s = \frac{(1-\nu^2)K_{Ic}^2}{2E} \tag{15}$$

The fracture surfaces predicted for 45 or 35 mm-high specimens with a threshold stress of 55 MPa and a critical stress of 110 MPa are plotted versus the amplitude of the thermal shocks in Fig. 22. Experimental data are also plotted for comparison.

The fracture surface is predicted to be smaller for 35 mm-high specimens than for 45 mm-high specimens, as expected from the comparison of the stresses in Fig. 10(c) and from the smaller volume in which to store elastic energy.

The values computed for tests 9 and 10 are in very good agreement with the measured values.

5. Conclusions

"Cold-to-hot" thermal shocks on cylinders constitute a convenient way to apply triaxial tension to a brittle material, with a possibility to vary the relative proportion of axial/radial/tangential stresses by changing the height-to-diameter ratio of the specimens.

The detection of a modification in the normal modes of vibration after thermo-mechanical loading of a specimen constitutes a fast and reliable method to detect the presence of internal damage in an opaque material.

Pores in a brittle material are more or less detrimental, depending on the local stress triaxiality. Roughly speaking, an increase in stress triaxiality reduces the harmfulness of the pore, not only in terms of stress concentration but also in terms of stress intensity factor when an annular crack initiates around it. Moreover, should two mutually orthogonal annular cracks initiate near the same pore due to equibiaxial tension, the stress intensity factor would be smaller than for a single crack under the same loading. The shielding effect would even be stronger for three mutually orthogonal annular cracks under triaxial tension.

The dynamic character of fracture in glass is responsible for fragmentation and makes crack paths predictions impossible from a quasi-static analysis of the stress field.

However, continuum damage mechanics can be used to predict the zone where cracks initiate and their initial orientations. The total crack surface can also be estimated from the dissipated energy associated with damage.

Acknowledgments

This study has been supported by Areva, Andra and the CEA. The authors are grateful to Dr. F. Bouyer from the CEA who provided the material, to J.C. Eytard for his assistance in vibration measurements and to Prof. J.J. Marigo for his advice concerning the computation of the fracture surface.

References

Barth, N., George, D., Ahzi, S., Rémond, Y., Doquet, V., Bouyer, F., Betremieux, S., 2012. Modeling simulation of the cooling process of borosilicate glass. J. Eng. Mat. Tech. Trans. ASME..

Barth, N., George, D., Rémond, Y., Ahzi, S., Doquet, V., Bouyer, F., in preparation. A 3D finite element damage model accounting for mode I opening in borosilicate glass.

Cotterell, B., Rice, J.R., 1980. Slightly curved or kinked cracks. Int. J. Fract. 16 (2), 155–169.

Cramer, T., Wanner, A., Gumbsch, P., 2000. Energy dissipation and path instabilities in dynamic fracture of silicon single crystals. Phys. Rev. Lett. 85 (4), 788–791.

Destuynder, P., Djaoua, M., Nedelec, J.C., 1981. Sur une interprétation mathématique de l'intégrale de Rice en théorie de la rupture fragile. Math. Methods Appl. Sci. 3 (1), 70–87.

Dube, M., Doquet, V., Constantinescu, A., George, D., Remond, Y., Ahzi, S., 2010. Modeling of thermal shock-induced damage in a borosilicate glass. Mech. Mater. 42, 863–872.

Faletti, D.W., Ethridge, L.J., 1988. A method for predicting cracking in waste glass canisters. Nucl. Chem. Waste Manage. 8, 123–133.

Goodier, J.N., 1933. Concentration of stress around spherical cylindrical inclusions flaws. J. Applied Mech. Trans. ASME. 55, A39.

Kamizono, H., Niwa, K., 1984. An estimation of the thermal shock resistance of simulated nuclear waste glass under water quenching conditions. J. Mater. Sci. Lett. 3, 588–590.

Lemaître, J., Chaboche, J.L., 1994. Mechanics of Solid Materials. Cambridge University press.

Mecholsky, J.J., 1995. Fractography: determining the sites of fracture initiation. Dent. Mater. 11, 113–116.

Quinn, J.B., 1999. Extrapolation of fracture mirror and crack-branch sizes to large dimensions in biaxial strength tests of glass. J. Amer. Ceram. Soc. 82 (8), 2126–2132.

Rabinovitch, A., Bahat, D., 2008. Mirror-mist transition in brittle fracture. Phys. Rev. E78, 067102-1–067102-4.

Sharon, E.S., Fineberg, J., 1999a. The dynamics of fast fracture. Adv. Eng. Mat. 1 (2), 119–122.

Sharon, E.S., Fineberg, J., 1999b. Confirming the continuum theory of dynamic brittle fracture for fast cracks. Nature 397, 333–335.

Shi, P., Ritter, J.E., Jakus, K., 1989. Effect of temperature on the mirror-mist constant of soda-lime and borosilicate glasses. Phys. Chem. Glasses 30 (1), 34–35.

Sun, X., Khaleel, M.A., 2004. Modeling of glass fracture damage using continuum damage mechanics – static spherical indentation. Int. J. Damage Mech. 13, 263–284.

Yoffe, E.H., 1951. The moving Griffith crack. Phil. Mag. 42 (330), 739–750.